Wind tunnel experiments to quantify the effect of aeolian snow transport on the surface snow microstructure

Benjamin Walter[1], Hagen Weigel[1], Sonja Wahl[2], and Henning Löwe[1]

[1]WSL Institute for Snow and Avalanche Research SLF, Davos, Switzerland
[2]School of Architecture, Civil and Environmental Engineering, École Polytechnique Fédérale de Lausanne (EPFL), Lausanne, Switzerland

Correspondence: Benjamin Walter (benjamin.walter@slf.ch)

Abstract. The evolution of the surface snow microstructure under the influence of wind is hardly understood but crucial for polar and alpine snowpacks. Available statistical models are solely parameterized from field data where conditions are difficult to control. Controlled experiments which exemplify the physical processes underlying the evolution of density or specific surface area (SSA) of surface snow under wind are virtually non-existing. As a remedy, we conducted experiments in a cold laboratory using a ring-shaped wind tunnel with an infinite fetch to systematically investigate wind-induced microstructure modifications under controlled atmospheric, flow and snow conditions. Airborne snow particles are characterized by high-speed imaging, while deposited snow is characterized by density and SSA measurements. We used a single snow type (dendritic fresh snow), cover wind speeds from 3 ms^{-1} to 7 ms^{-1} (for fixed temperature) and vary temperatures from -24°C to -2°C (for fixed wind speed). The measured airborne impact trajectories confirm the consistency of our coefficient of restitution with large scale saltation, rendering the setup suitable to realistically study interactions between airborne and deposited snow. Our measured densification rates in the deposit as a function of wind speed show clear deviations from existing statistical models, but can be re-parameterized through our data. The most drastic changes in densification and SSA rates of deposited snow are observed close to the melting point. This study, as a first of its kind, exemplifies a rich non-linear interplay between airborne and deposited snow particles which is discussed in view of a multitude of involved processes, i.e. airborne metamorphism, cohesion, particle separation and fragmentation.

1 Introduction

The topmost centimeters of a snowpack (herein referred to as "surface snow") forms the interface to the atmosphere and is frequently affected by wind (e.g., Seligman, 1936; Mott et al., 2018). During a snowstorm, the typically dendritic precipitation particles with diameters of 1-5 mm (Woods et al., 2008; Garrett and Yuter, 2014) are subject to aerodynamic drag forces. Depending on wind speed and particle size and shape, the snow particles either roll on the ground (rolling), follow near ground ballistic trajectories occasionally impacting on the ground (saltation), or are transported without contacting the ground (suspension) (e.g., Walter et al., 2014). Snow particle fragmentation upon surface collisions during saltation (Sato et al., 2008; Comola et al., 2017), rounding due to abrasion while rolling, and sublimation in sub-saturated air (Dai et al., 2014) are key factors determining the size, shape and packing density (Golubev and Sokratov, 2004; Cho et al., 2006) of the ultimately de-

25 posited snow. Blowing snow particles are typically smaller than precipitation crystals (Schmidt, 1982; Nishimura and Nemoto, 2005; Nishimura et al., 2014), with diameters ranging from 50–500 μm and with a higher sphericity and lower dendricity (Bartlett et al., 2008). The deposited snow particles define the microstructure and thereby the properties of surface snow like albedo, density, or cohesion. These properties are relevant for the mechanical stability of wind slabs for avalanche formation (Schweizer et al., 2003), the exchange of chemical species with the atmosphere (e.g., Pomeroy and Jones, 1996), alpine and

30 polar mass balances (Rignot and Thomas, 2002), or radiative transfer (Flanner and Zender, 2006). Thus, it is critical for models of different spatial resolution from process based snowpack models to global scale climate models to accurately simulate how the physical properties of the snow surface change under the influence of wind.

The physical properties of snow are mainly dominated by two snow microstructural parameters: i) the snow density $\rho_s = \rho_i \phi_i$, where $\rho_i = 917 \, \mathrm{kg\,m^{-3}}$ is the density of ice and $0 < \phi_i < 1$ is the ice volume fraction of snow, and ii) the specific surface area

35 (SSA) defined as the surface area per ice mass (or volume) (e.g., Proksch et al., 2015; Warren, 2019). Surface snow densities range from 70-100 $\mathrm{kg\,m^{-3}}$ for Alpine fresh snow deposited under weak wind conditions, up to typically 200-300 $\mathrm{kg\,m^{-3}}$ for strongly wind affected surface snow in Arctic and Antarctic regions (Brun et al., 1997). The SSA of surface snow ranges from 70-150 $\mathrm{mm^{-1}}$ for fresh snow (Yamaguchi et al., 2019) to 20-40 $\mathrm{mm^{-1}}$ for strongly wind affected snow in Antarctica (Gallet et al. 2010). For stationary surface snow under isothermal temperature conditions, the density increases and the SSA decreases

40 over time (Schleef et al., 2014a). Wind generally results in an increase of the surface snow density (Seligman, 1936, Sokratov and Sato 2001, Liston et al. 2007, Vionnet et al., 2012) with densification rates that are one to two orders of magnitude higher than for isothermal metamorphism (Liston et al. 2007). Available statistical models (Lehning et al., 2002, Liston et al. 2007, Vionnet et al., 2012) for the increase of surface snow density due to wind are exclusively based on field measurements that are difficult to control and limited by the problem of accurately measuring snow transport and microstructure simultaneously.

45 Recently, Domine et al. (2019) found that the snow models SNOWPACK (Lehning et al., 2002) and Crocus (Vionnet et al., 2012) greatly underestimate the increase in snow density for Arctic surface layers. Cabanes et al. (2003) found that wind increases the rate of SSA decrease, but insufficient data prevented a parametrization of this effect. To the best of our knowledge, no other study yet investigated the effect of wind on the SSA.

Different physical processes occurring during aeolian snow transport like particle fragmentation, sublimation and water va-

50 por re-deposition, may be responsible for the increase in deposited snow density and SSA changes. Snow densification by wind is believed to be mainly the consequence of particle fragmentation resulting in higher packing densities of the ultimately deposited blowing snow particles (Sato et al., 2008; Comola et al. 2017). Fragmentation of snowflakes may already occur at low wind velocities (Sato et al., 2008). For wind velocities $< 2 \, \mathrm{m\,s^{-1}}$, highly dendritic precipitation snowflakes were found to not break upon collision with the surface, whereas they are completely decomposed for wind velocities $> 5 \, \mathrm{m\,s^{-1}}$. The

55 number of fragments increased while the fragment size decreased with impact velocity (Sato et al., 2008). A discrete element model (DEM) of the fragmentation process was presented by Comola et al. (2017), linking the size distribution of blowing snow particles to that of falling snow crystals. Pure sublimation of windblown snow particles results in a reduction of snow particle size, and partial disappearance of entire grains, potentially resulting in a significant mass loss (Groot-Zwaaftink et al., 2013, Palm et al. 2017). Vapor deposition at suspended particles, contrarily, results in increasing particle sizes, an effect

60 which increases with increasing air temperature (Yamaguchi et al., 2019). To discern the different processes, it is inevitable to complement field measurements by controlled laboratory experiments.

It is the aim of our study to propose an experimental setup to systematically investigate how wind affects the evolution of the surface snow density and SSA as functions of the wind speed, air temperature and transport duration. We therefore deployed a ring-shaped wind tunnel (RWT) in a walk-in cold room to combine flow measurements (velocity, temperature, hu-

65 midity) and particle characteristics (coefficient of restitution, impact angle and velocity) with established snow microstructure measurements (X-ray tomography, IceCube, density cutter) under controlled cold laboratory conditions. The relevant physical processes responsible for the density and SSA changes, i.e., particle fragmentation, sublimation and vapor re-deposition are characterized and linked to the surface snow microstructure modifications.

The manuscript is organized as follows. The methods, instrumentation and models used and tested in this study are in-

70 troduced in Section 2. The density and SSA measurements, high-speed camera particle imaging, and the microstructural modifications due to wind are introduced, discussed, and compared to the models in Section 3. A summary of the results, the main conclusions and an outlook can be found in Section 4.

2 Methods

2.1 Ring wind tunnel

75 Experiments using a closed-circuit RWT were performed under stable temperature conditions in one of the WSL/SLF cold labs in Davos (Switzerland). The RWT (Fig. 1a) has an obround shape with two straight sections providing space for measurements without centrifugal effects as they occur in the curved sections. The RWT system is 2.2 m long and 1.2 m wide, and its tunnel is 20 cm wide and 50 cm high (Sommer et al., 2017). A model-aircraft propeller driven by an electric motor is used to create the airflow. The propeller is controlled by the wind velocity $V_{0.4m}$ measured at a height of 0.4 m to maintain a target wind

80 velocity. In the empty RWT without snow, the maximum possible wind speed is approximately $V_{0.4m} \approx 8.5$ ms^{-1}. The infinite fetch of the closed-circuit RWT enables continuous snow transport with particles rolling or saltating on the ground, or being in suspension for longer time periods. This is not possible in open-circuit wind tunnels like the large-scale wind tunnel at WSL/SLF (e.g., Walter et al., 2012a-c), where particles are blown out of the tunnel after a few seconds of transport.

2.2 Drift experiments

85 For the drift experiments, dendritic fresh snow was produced in the WSL/SLF snowmaker (Schleef et al., 2014b) at an air temperature of -20°C and a water bath temperature of +30°C, resulting in initial snow densities of 45-80 kgm^{-3} and SSA of 45-70 mm^{-1} for the experiments. For each of the twelve main experiments, a constant wind velocity was initially set ranging in between $V_{0.4m}$ = 4 - 7.1 ms^{-1} (Table 1). A total volume of (60 x 40 x 40 cm^3) of fresh snow was then slowly added to the wind tunnel, temporally equally distributed over the entire experiment duration τ_{exp} (Table 1), to mimic snow precipitation

90 until the end of the experiment. The new snow was carefully poured into the wind tunnel at an inlet (Fig. 1a) with a shovel,
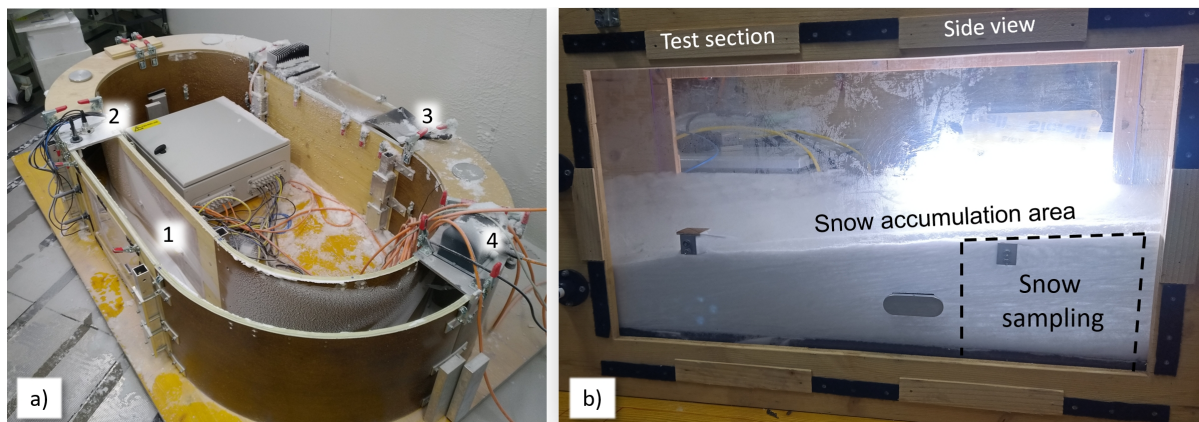
Figure 1. a) RWT installed in the cold laboratory at T_a = -20°C: 1) Straight test section, 2) Measurement section with snow and air temperature, relative humidity, and wind speed sensors, 3) Inlet for adding fresh snow and 4) Wind turbine. b) Side view of the test section with the snow accumulation area where the snow microstructure measurements were performed.

minimizing the destruction of the initial microstructure. Only the microstructure of the snow crystals getting into contact with the shovel may be slightly affected by the pouring procedure, while their quantity is negligible compared to the entire volume of snow on the shovel. No sieving was applied to avoid preceding fragmentation of the highly dendritic snow crystals. Once a portion of new snow was poured into the RWT, it got immediately suspended and redistributed in the flow. The new snow

95   in the Snowmaker box that served as the initial condition for the experiments, is regarded as the microstructure representing precipitation deposition unaffected by wind ($V_{0.4m}$ = 0 m s^{-1}). The settings and atmospheric conditions for the twelve experimental runs are summarized in Table 1. For the experiments 1-7, the wind velocity ranged from $V_{0.4m}$ = 4 – 7.1 m s^{-1} while the transport duration (0.5 h) and the air temperature ($\approx$ -22 $\pm$1°C) were constant. For the experiments 8-12, the wind velocity was set to $V_{0.4m}$ = 6 m s^{-1} while the experiment duration was varied (τ_{exp} = 1 h and 2.5 h, experiments 8 and 9) or the air

100 temperature was changed to T_a = -12°C, -6°C and -2°C (experiments 10 – 12). The major snow accumulations analyzed with the instruments discussed in the following Section developed in the straight test section of the RWT (Fig. 1b).

Two complementary experiments were conducted to i) measure and analyze particle impact characteristics and ii) to separately investigate the effect of long snow transport durations. Both experiments were conducted at an air temperature of $T_a \approx$ -20°C while a low mass of snow (600g) was poured into the RWT at the beginning of the experiment. For experiment i) The

105 wind speed was varied from $V_{0.4m}$ = 3 – 7 m s^{-1} and near surface particle impacts were recorded with a high-speed camera (Experiment 13 in Table 1). A total of 75 particle impacts were recorded for the different wind velocities. For experiment ii) the wind speed was set to $V_{0.4m}$ = 8 m s^{-1} to keep the particles in suspension as long as possible, and the transported particles were sampled out of the air every 15 min (Experiment 14 in Table 1).

Table 1. Overview of the experimental settings and atmospheric conditions for the main experiments (1-12) and the complementary experiments (13-14). The average value for RH is calculated from the second period of each experiment where a situation close to equilibrium for RH is reached (Fig. 2).

Experiment	Mean wind speed $V_{0.4m}$ $[ms^{-1}]$	Experiment duration τ_{exp} $[h]$	Average air temperature T_a [°C]	Average relative humidity RH [%]
1	5.0	0.5	-24.0	92.0
2	6.9	0.5	-24.6	99.5
3	6.0	0.5	-23.8	99.5
4	7.1	0.5	-21.3	99.5
5	4.0	0.5	-20.6	98.6
6	6.6	0.5	-20.6	98.7
7	5.0	0.5	-23.1	98.5
8	6.0	1.0	-21.7	98.1
9	6.0	2.5	-21.0	100.7
10	6.0	0.5	-11.5	100.5
11	6.0	0.5	-5.6	99.9
12	6.0	0.5	-2.4	99.4
13	3.0 - 7.0	5.8	-20.6	83.5
14	7.9	2.5	-18.0	98.5

2.3 Instrumentation and measurements

The straight test section (Fig. 1a and b) is equipped with various sensors for continuously measuring the air temperature T_a (HC2-S, Rotronic, uncertainty: ±0.3°C), the relative humidity RH (HC2-S, Rotronic, uncertainty: $\pm1.5\%$) and the wind speed $V_{0.4m}$ (MiniAir, Schildknecht, uncertainty: ±0.2 ms^{-1}). The atmospheric data is sampled at a frequency of 5 Hz using a custom-made software based on LabVIEW (National Instruments). A high-speed camera (Phantom, Vision Research) is used to record particle impacts close to the snow surface and to calculate particle impact characteristics like the coefficient of restitution and impact and ejection angles.

Snow microstructure measurements were performed before and after the drift experiments to characterize the fresh and the wind affected surface snow microstructures. An IceCube (A2 Photonics Sensors) instrument was used to measure the specific surface area of the snow samples with a stated measurement uncertainty of $\pm10\%$ (Gallet et al., 2009). Recently reported systematic IceCube measurement errors detected for SSA < 20 mm^{-1} (Martin and Schneebeli et al., 2023) are unproblematic for our dendritic fresh snow experiments with SSA > 20 mm^{-1}. Micro-computed tomography (μCT) measurements of the initial and final snow microstructures were performed for the experiments 5-12 to access information on particle size distributions and to obtain complementary measurements of the SSA and the snow density. A cylindrical snow sample with a diameter of 36 mm

and a height of 70 mm was vertically cut out of the initial new snow or the accumulated snow for the μCT measurements. The

125 μCT measurements for the main experiments (Experiments 1-12, Table 1) were performed with a Scanco CT-40 scanner with a

voxel size of 18 μm (e.g., Pinzer and Schneebeli, 2009; Heggli et al., 2011). The rather low resolution is chosen because of the

necessity of using sufficiently large sample holders for taking snow samples from the deposit. For smaller sample holders, an

impact of sampling on the density is unavoidable for the densities of interest. Therefore it cannot be ruled out that absolute val-

ues of the SSA are biased low due to resolution. A smaller sample holder was used for the additional Experiment 14 resulting

130 in a voxel size of 8 μm. For the binary segmentation, the energy-based segmentation procedure presented by Hagenmuller et al.

(2013) was used. A marching cubes approach (Hagenmuller et al., 2016) is used for calculating the SSA from the segmented

μCT images. A standard density cutter (5.5 x 6 x 3 cm^3) was used to measure the snow density. The cutter and μCT density

measurements were found (Proksch et al., 2016) to agree within 5-9%, thus resulting in a similar overall uncertainty for the

density and for the SSA measurements.

135 ## 2.4 Densification models

To make contact to field-based results, two available model formulations for snow densification (SNOWPACK, Lehning et

al., 2002, and SnowTran-3D, Liston et al., 2007) are tested in our study. In Lehning et al. (2002), a relationship between the

wind velocity, air temperature, relative humidity and snow density used in SNOWPACK was derived by relating local weather

station data to snow density measurements in an alpine catchment:

140 $$\rho_s = 10^{\beta_0 + \beta_1 T_a + \beta_2 \arcsin(\sqrt{RH}) + \beta_3 \log_{10}(V)} \tag{1}$$

In Eq. 1, β_0 = 3.28, β_1 = 0.03, β_2 = -0.75 and β_3 = 0.3 are constants, T_a is the air temperature in [°C], RH is the dimensionless

relative humidity varying between 0 and 1, and V the wind velocity at 2 m height in [m s^{-1}]. In contrast, Liston et al. (2007)

describes the evolution of the surface snow density during periods of precipitation as a function of the temperature dependent

new snow density ρ_{ns} plus a wind-related density offset for wind speeds > 5 m s^{-1}:

145 $$\rho_s = \rho_{ns}(T_{wb}) + D_1 + D_2[1 - e^{-D_3(V-5)}] \tag{2}$$

In Eq. 2, D_1 = 25, D_2 = 250 and D_3 = 0.2 are constants, T_{wb} the wet-bulb air temperature in [K] and V the wind speed at 2

m height in [m s^{-1}]. Another empirical description of surface snow affected by wind is implemented in the CROCUS snow

model (Brun et al., 1997; Vionnet et al., 2012). However, as the model uses the parameters sphericity and dendricity which are

difficult to quantify, an analysis of the performance of their model is not part of this study.

150 ## 3 Results and discussion

3.1 Atmospheric and flow conditions

The air temperature (T_a), relative humidity (RH), and wind speed ($V_{0.4m}$) are continuously measured and provide a basis for

the surface snow microstructure analysis and discussion. The air temperatures typically increased by about 1-2°C during an
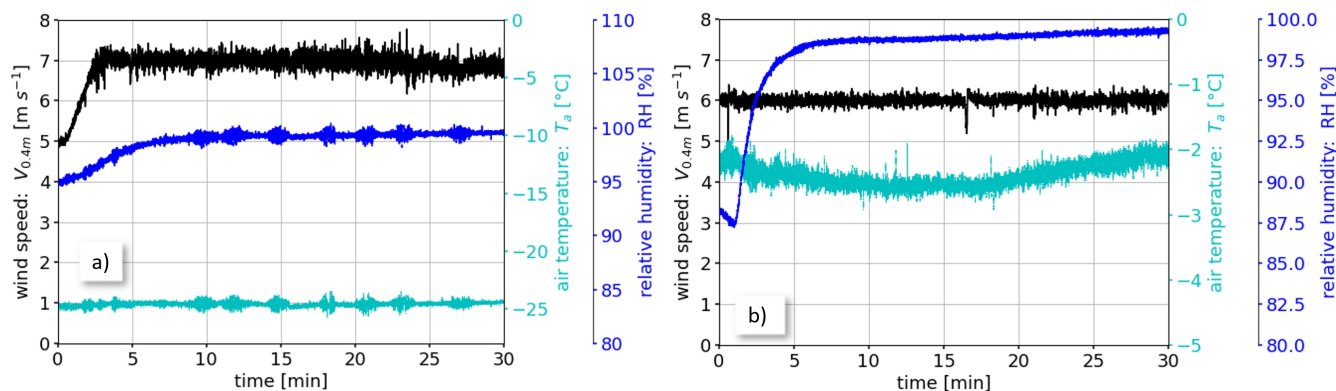
Figure 2. a) Evolution of the atmospheric conditions for experiment a) 2 and b) 12 including the wind speed ($V_{0.4m}$), air temperature (T_a) and relative humidity (RH).

experiment due to turbulent energy dissipation in the flow and heat generated by the turbine (Fig. 2). The RWT is not sealed,

155 and air is exchanged between the RWT and the cold lab mainly at the inlet where the fresh snow was poured into the RWT (Fig. 1a). The relative humidity typically increased significantly by about 5-10% during the first 5-10 min of the experiments due to sublimation of snow particles in suspension and at the snow surface. Afterwards, an equilibrium situation is reached between sublimation and dry air exchange between the RWT and the cold lab at the inlet resulting in a rather stable or minor increase of RH until the end of the experiment. In Fig. 2, RH is shown with respect to ice and thus typically close to saturation during

160 the second half of the experiments.

3.2 Particle transport characteristics

To make contact to previous studies of well-developed boundary layer flows we address the consistency of particle transport and impact characteristics. A known limitation of the closed-circuit RWT is, that the deflection of the flow in the curved sections and the small tunnel cross-section prevents the development of a stable logarithmic boundary layer flow (Sommer et al.,

165 2017) which is indeed critical for flow properties. In contrast, for this study, it is important that the relevant particle transport properties, i.e. the particle impact angles and velocities in the saltation layer are comparable to those of a fully developed natural boundary layer flow. These particle properties drive particle fragmentation, abrasion, and sublimation, and therefore the interaction with the microstructure of the ultimately deposited snow. We therefore argue here that the boundary layer flow may not necessarily be perfectly homogeneous, stationary, and well-developed, as long as the particle impact characteristics

170 are consistent with natural conditions. Using the high-speed camera setup we measured particle impact angles, ejection angles and velocities for a wide range of different wind speeds (Experiment 13 in Table 1).

An image sequence of a dendritic snow particle impacting on a snow surface recorded with a high-speed camera is shown in Fig. 3 as an exemplary case. The incoming particle merely rotates before the impact (Fig. 3a). The vertical ($V_{in,y}$) and horizontal ($V_{in,x}$) particle velocities define the absolute impact velocity V_{in}. Fig. 3b shows the situation at the time where the
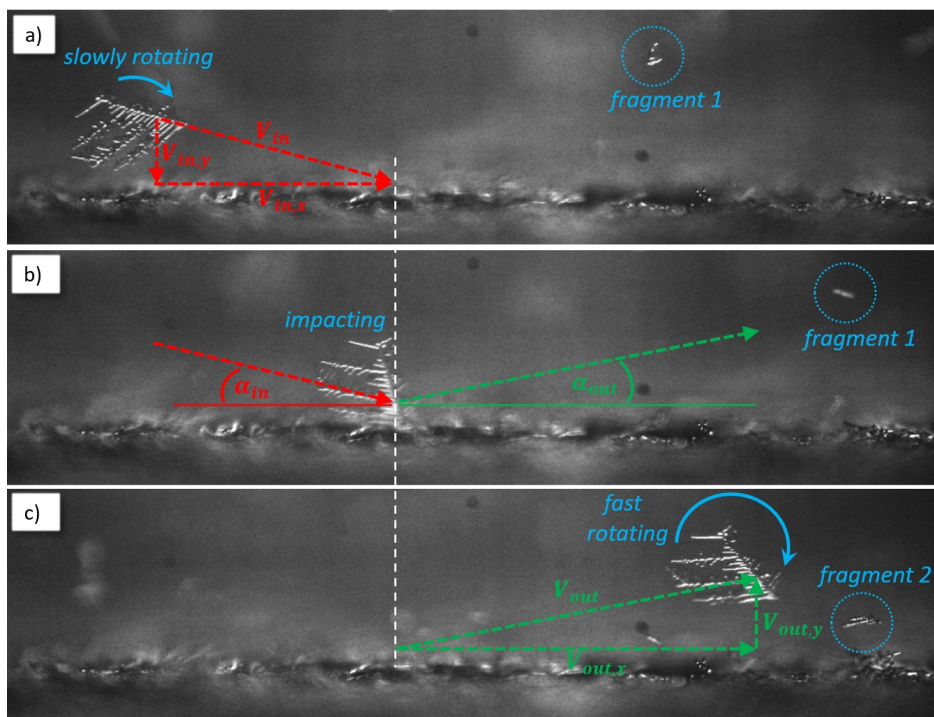
Figure 3. High-speed camera recording of a dendritic new snow particle impacting on a snow surface for an experiment with a wind speed of $V_{0.4m} = 6$ m s^{-1}. a) The particle slowly rotates before impacting at the surface with an impact velocity V_{in}. b) The particle impacts with the surface at an impact angle α_{in} and leaves the surface at an ejection angle α_{out}. c) the particle is ejected at a different, lower ejection velocity V_{out} and is fast rotating. Furthermore, two different fragments being transported by the wind are shown.

175   particle is in contact (impacting) with the stationary snow surface. The impact angle α_{in} and the ejection angle α_{out} are defined by the incoming and outgoing particle trajectories. Depending on the amount of energy that is dissipated or transformed on impact, the particle is ejected at a lower ejection velocity V_{out} (Fig. 3c). In this case, no fragmentation of the impacting particle happened, however, the ejected particle is strongly rotating after the impact. Additionally, two different fragments that are transported by the wind are shown in the three images of Fig. 3.

180   The energy dissipation upon particle impact can be quantified through the apparent coefficients of restitution. The relevant collision quantities, the impact velocities ($V_{in} \approx$ 1-5 m s^{-1}), the impact angles ($\alpha_{in} \approx$ 1-20°) and the vertical ($C_v = V_{out,y}$ / $V_{in,y}$) and horizontal ($C_h = V_{out,x}$ / $V_{in,x}$) coefficients of restitution (Fig. 4) compare well with those measured by (Sugiura et al., 2000) in a large-scale boundary layer wind tunnel under well developed and stationary flow conditions. The values for the vertical coefficient of restitution are in the range of $C_v \approx$ 0.5-18 (Fig. 4a) which are slightly higher than those found by

185 Sugiura et al. (2000), who measured values for $C_v \approx$ 1-3. The reason for this difference is our high-speed camera setup that allowed for high resolution images close to the ground (Fig. 3) and thus the detection of very low impact and ejection angles down to $\alpha_{in} = 1°$ (Fig. 4b), while the data of Sugiura et al. (2000) is limited to $\alpha_{in} > 5°$. Particles with low impact angles and
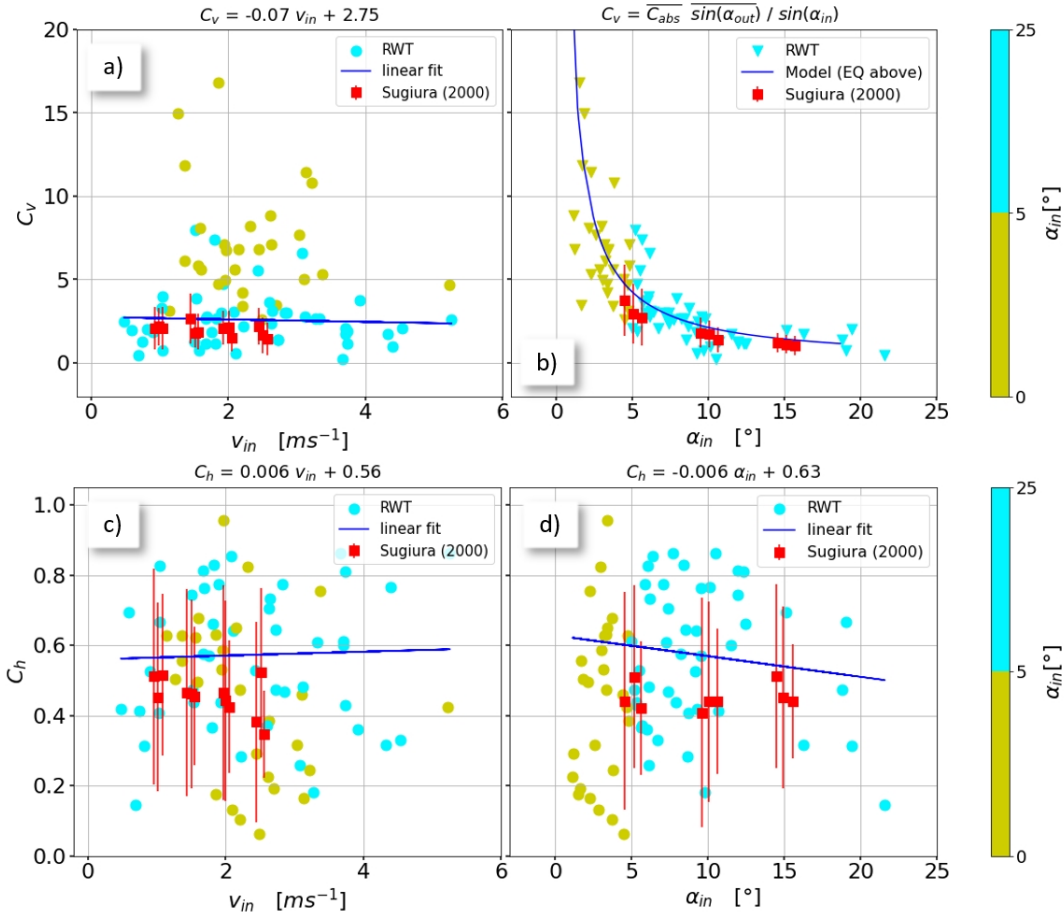
Figure 4. Vertical C_v (a and b) and horizontal C_h (c and d) coefficients of restitution as functions of the impact velocity V_{in} (a and c) and the impact angle α_{in} (b and d). Note: Our RWT data is color coded to visualize the agreement with Sugiura et al. (2000) for $\alpha_{in} > 5°$.

high ejection angles result in high vertical coefficients of restitution C_v (yellow dots in Fig. 4) and explain the difference to Sugiura et al. (2000). For C_v we find a clear dependence on the impact angle α_{in}, similar to Sommerfeld et al. (2021), which

190 can be cast into the form:

$$C_v(\alpha_{in}) = \overline{C_{abs}} \, \overline{\sin(\alpha_{out})} \, \sin^{-1}(\alpha_{in}) \tag{3}$$

Eq. 3 is plotted in Fig. 4b with $C_{abs} = |V_{out}|/|V_{in}|$ (Fig. 5b). For a better comparability of our horizontal and vertical coefficients of restitution with the results of Sugiura et al. (2000), the linear fits shown in Fig. 4a, c and d are limited to the collisions with $\alpha_{in} > 5°$. Our horizontal coefficients of restitution span the same range of $C_h \approx 0.1$ - 0.9 (Fig. 4c-d) as those found by

195 Sugiura et al. (2000). These collision quantities (C_v and C_h) define the forces acting on the dendrites or branches of the fresh snow particles during an impact and thus the degree of fragmentation (Comola et al., 2018).

To complete this impact analysis, we show in Fig. 5a that the average impact velocity V_{in} increases with increasing wind
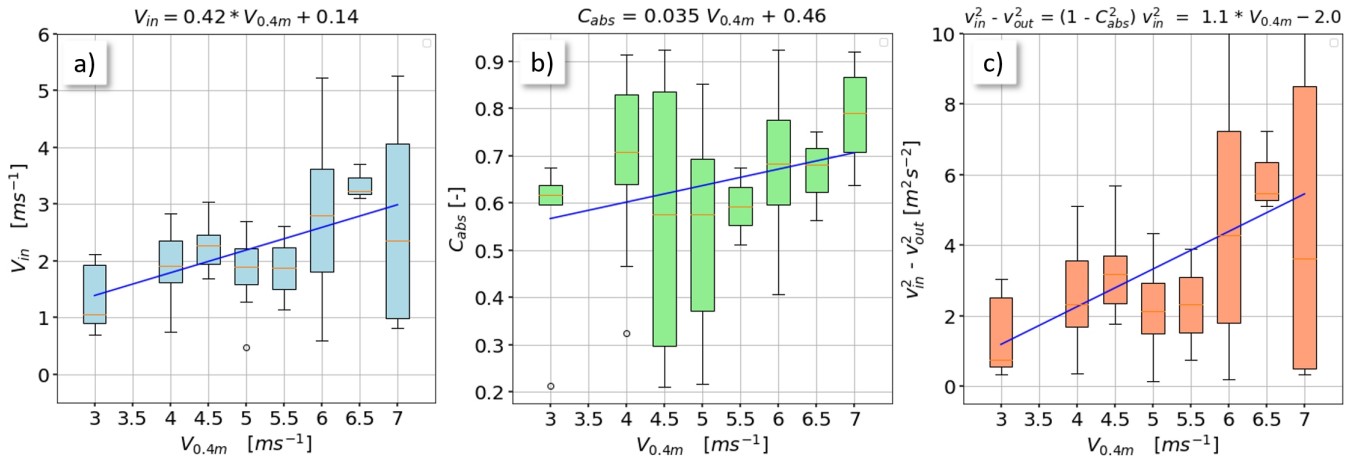
Figure 5. a) Particle impact velocity V_{in}, b) absolute coefficient of restitution C_{abs} and c) normalized dissipated impact energy $V_{in}^2 - V_{out}^2$ as a function of the RWT wind speed $V_{0.4m}$.

speed $V_{0.4m}$. Fig. 5b demonstrates that, despite considerable scatter, the absolute coefficient of restitution C_{abs} slightly increases with wind speed $V_{0.4m}$. This implies that the total energy available for the densification processes, the normalized
200 dissipated impact energy $V_{in}^2 - V_{out}^2$ increases with wind speed (Fig. 5c).

A visual inspection of the saltation layer shows a typical saltation layer height of $h_{salt} \approx$ 30 - 50 mm with a homogeneous particle distribution across the RWT cross-section in the straight test section (not shown here). Comparable saltation layer heights were measured for well-developed natural boundary layer flows in the large-scale wind tunnel using shadowgraphy imaging (Gromke et al., 2014). The particle concentration in the RWT also exponentially decreases with height as shown
205 by the measurements of Yu et al. (2023) while studying snow cornice formation in the same RWT. In the curved sections, a large portion of the snow particles are transported along the outer wall due to centrifugal forces. The smallest particles are transported in suspension without contacting the snow surface and are partially blown out of the wind tunnel at the inlet. Overall, the results of this Section emphasize that our boundary layer flow is sufficiently developed which substantiates the feasibility of quantifying the effect of wind on the surface snow microstructure using the RWT.

210 ### 3.3 Snow density and SSA measurements

An increase in snow density is measured for all experiments while the magnitude of the increase depends on the flow and atmospheric conditions (Fig. 6a-b). The horizontal and vertical density variability across the wind tunnel width was measured with the density cutter for 2-3 profiles in flow direction at the snow accumulation area (Fig. 1b), resulting in a total of 5-30 density measurements for each experiment depending on the amount and height of the snow accumulation. The initial new snow
215 densities representing snow deposited without wind ($V_{0.4m} = 0$ m s^{-1}) measured inside the Snowmaker box were ranging in between 45-80 kg m^{-3} (Fig. 6a-b) while these densities increased after wind exposure to values ranging from 75-350 kg m^{-3},
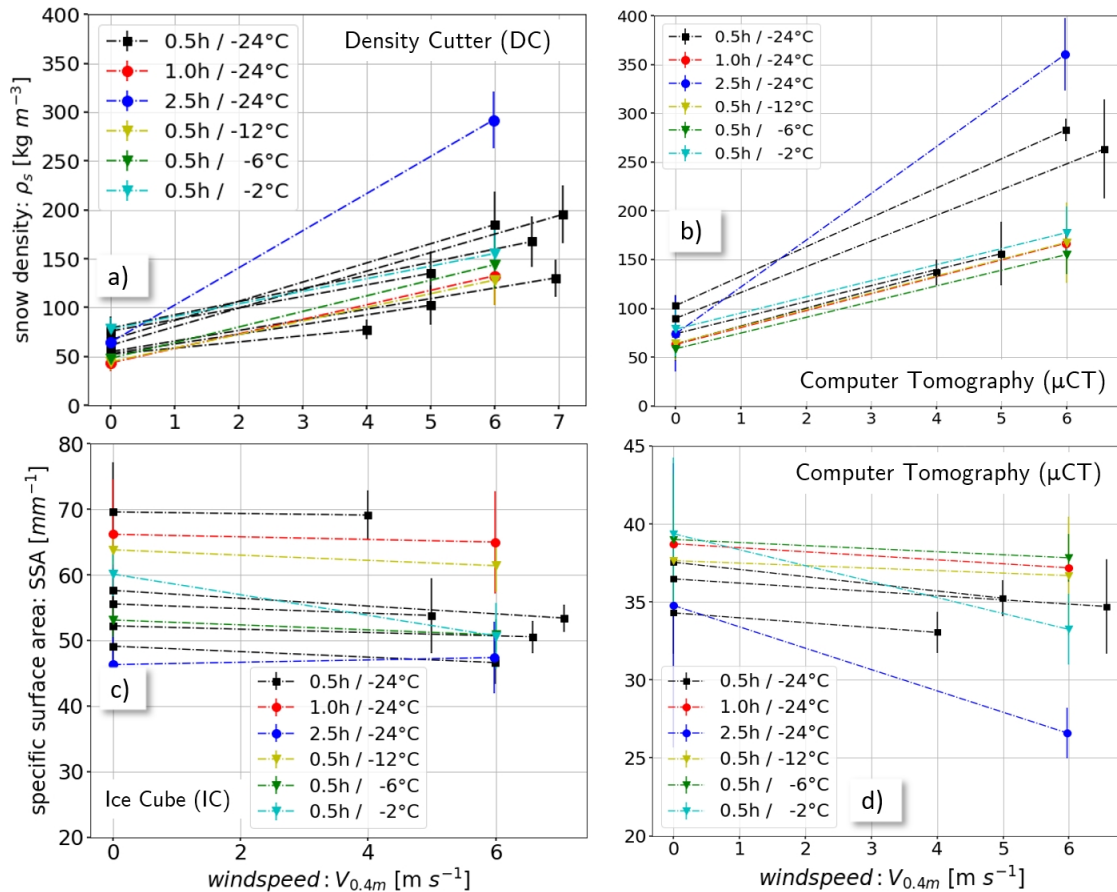
Figure 6. Summary of the snow densities measured with a) the density cutter and b) μCT, and the specific surface area measured with c) the IceCube instrument and d) μCT as a function of the windspeed $V_{0.4m}$. $V_{0.4m} = 0\,ms^{-1}$ corresponds to the initial new snow from the Snowmaker box. The error bars indicate one standard deviation of the variability (including spatial variability) of the measurements.

depending on the wind speed, air temperature and transport duration. An overall good agreement with strongly increasing densities for both, the cutter (Fig. 6a) and the μCT (Fig. 6b) measurements is found for the experiments 5-12 where μCT measurements are available. However, differences of up to 20% between the individual experiments are attributed to general

220 differences between the two methods as described in Section 2.3 and the spatial variability (Fig. 7) which is not accounted for by the single μCT sample.

The corresponding SSA values measured with the IceCube and μCT are shown in Fig. 6c-d, both indicating a reduction in the SSA values due to wind exposure. The initial new snow SSA values are ranging from 45 mm^{-1} < SSA < 70 mm^{-1} for the IceCube measurements, whereas lower values of 35 mm^{-1} < SSA < 40 mm^{-1} were measured with the μCT. The lower

225 μCT values are partially the result of the μCT resolution with a voxel size of 18 μm as discussed in Section 2.3. Differences between IceCube and μCT measurements may also be based on other reasons like the μCT SSA computation algorithm or
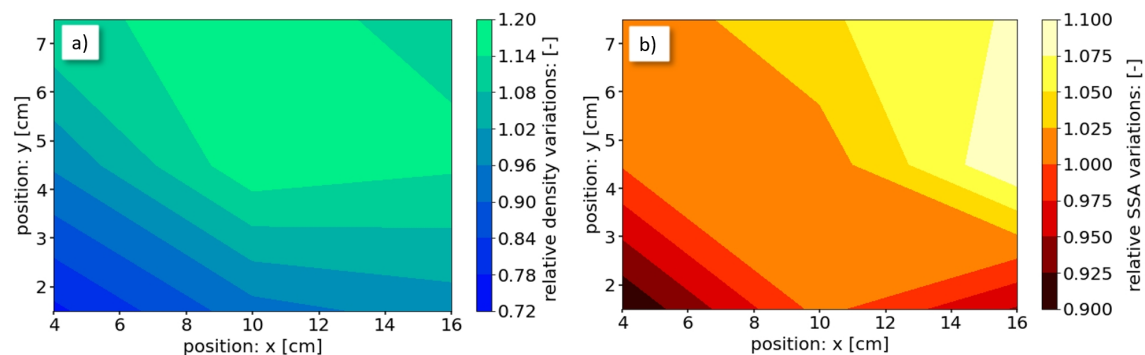
Figure 7. Average of the spatial variability of a) the snow density measured with the density cutter, and b) the SSA measured with the IceCube instrument. Position $x = 4$ cm corresponds to the inside wall of the RWT, so the view is in flow direction.

grain shape (Hagenmuller et al., 2016). However, the relative changes (e.g. SSA rates in Fig 11b) are consistent between the IceCube and μCT measurements. Because the aim of this study is the investigation of relative changes in the snow density and SSA induced by wind, the discrepancy in the absolute SSA values is not necessarily a problem but must be considered

230 carefully for the interpretation of the results. The error bars in Fig. 6 include, besides systematic and statistical measurement uncertainties, also the spatial variability (Fig. 7) of the snow density and SSA in the accumulation area (Fig. 1b).

Fig. 7 shows the vertical and horizontal density and SSA variations across the wind tunnel cross-section averaged for all experiments. The variability is first normalized by the mean for each experiment before an average of all 12 (10 for the SSA) experiments is calculated. The density varies about +/- 25% relative to the mean, with the lowest densities at the lower left

235 of the vertical snow profiles which corresponds to the inside wall of the RWT at $x = 4$ cm. The wind velocities are lowest at this location where the first, thus least fragmented snow accumulations with rather low densities appear. While the snow accumulations grow during the experiment, the densities tend to increase with height and towards the outer wall at $x = 16$ cm. Increasing densities with height can be explained by the gentle slope that forms during the experiment facing the wind (Fig. 1b). Sommer et al. (2018) found increasing densities with increasing slope angle of the snow cover because of steeper snow

240 particle impact angles and thus most likely enhanced fragmentation and higher packing densities.

The spatial SSA variability is overall smaller compared to the density with +/-10 % variation across the wind tunnel cross-section (Fig. 7b). The smallest SSA values are found at the lower left corner at $x = 4$ cm while the SSA increases towards the upper right. One explanation could be that initially the smallest fragments sublimate due to the low relative humidity (Fig. 2) and that the largest particles from the added new snow accumulate first, resulting in initial snow accumulations with a

245 rather low SSA. However, the measured spatial SSA variability is of the same order of magnitude as the SSA measurement uncertainty (Section 2.3).

3.4 Snow densification rate

The snow densification rate describes the temporal increase in density relative to the initial snow density and is defined as ϕ_{rate} = (ϕ_i - ϕ_{i0}) / ($\phi_{i0}\,\Delta t$), where (ϕ_{i0}) is the initial and (ϕ_i) the final ice volume fraction after a time duration Δt where snow trans-
250 port occurs. To understand the origin of snow densification we consider the kinetic energy loss by impacting particles which can only be transformed into rotational kinetic energy (Fig. 3), friction (heat), bed compression, or abrasion and fragmentation. Rotation and friction (heat) cannot be responsible for densification. The pressure that saltating particles exert on the snow surface resulting in bed compression can be estimated from the particles momentum difference before and after the impact. An upper limit for this pressure estimate includes the assumptions of ice spheres of 0.5 mm diameter, purely vertical impacts, a
255 maximum velocity difference of 3 m s^{-1} before and after the impact, and 10 impacts per square centimeter and second. The maximum pressure estimate of 0.02 Pa is too low to result in a significant bed compression and thus snow densification when being compared to the pressure of 133 Pa that was applied to a snow surface during the compaction experiments of Schleef et al. (2014a). Therefore, fragmentation and abrasion resulting in smaller particles and thus higher packing densities (Parteli et al., 2014) are assumed being the major processes behind wind induced surface snow densification. This conclusion is also
260 supported by the findings of Sato et al. (2008), showing that snow flakes are completely decomposed when impacting a surface for wind speeds > 5 m s^{-1} during precipitation.

3.4.1 Dependence on wind speed and involved mechanisms

Fig. 8 summarizes the densification rates for the experiments with different wind velocities (Table 1) which are derived from the averages of the density cutter and the μCT measurements weighted by their sampling volume. Furthermore, Fig. 8 includes
265 model predictions and model fits to our RWT data using the theoretical descriptions from Lehning et al. (2002) and Liston et al. (2006) (Eq. 1 and 2). The densification rates for the experiments (black squares in Fig. 8) show an increase with increasing wind speed from ϕ_{rate} = 1.3 − 4.3 h^{-1}. These rates are two to three orders of magnitude higher than those measured for isothermal metamorphism by Schleef et al. (2014a), which underlines the effect of wind.

Comola et al. (2017) showed that the average fragment size decreases and the number of fragments increases with increasing
270 particle impact velocities V_{in}. As V_{in} was found to increase with increasing wind speed $V_{0.4m}$ (Fig. 5a), we assume that also in our case the fragment size decreases and the packing density increases with increasing wind velocity $V_{0.4m}$, thus being responsible for the observed densification rate increase shown in Fig. 8. Furthermore, stronger fragmentation at higher wind velocities requires higher impact energies being dissipated by plastic deformation of snow crystals. To test this assumption, and therefore also the simulated results of Comola et al. (2017), the dissipated impact energy is estimated by calculating the
275 normalized kinetic energy difference $V_{in}^2 - V_{out}^2 = (1 - C_{abs}^2)V_{in}^2$ before and after the particle impacts. Fig. 5c shows that the dissipated impact energy increases with increasing wind velocity $V_{0.4m}$ (despite an increase of the absolute coefficient of restitution shown in Fig. 5b), likely resulting in smaller fragments, higher packing densities and thus stronger densification. The quality and resolution of the high-speed camera recordings did, however, not allow for analyzing individual particle impacts on fragmentation.
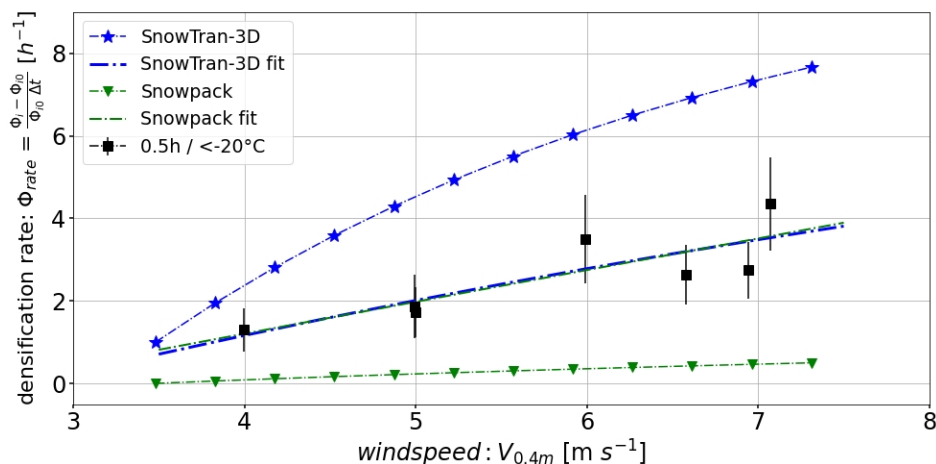
Figure 8. Densification rate as a function of wind speed for the Experiments 1-7 with constant air temperature ($T_a \approx$ -24°C) and experiment duration (τ_{exp} = 0.5 h) including the results of the SnowTran-3D (Liston et al., 2007) and the SNOWPACK (Lehning et al., 2002) model predictions and model fits to our experiments.

3.4.2 Comparison to models

Our data facilitates a direct comparison to the predictions from SNOWPACK (Eq. 1, Lehning et al., 2002) and SnowTran-3D (Eq. 2, Liston et al., 2007). Both models (Fig. 8) predict an increase with wind speed, however, significantly different from each other and from our measurements when the original parameters are used. Both models are parameterized from field measurements, where simultaneous flow and microstructure measurements in unstable wind conditions with intermittent snow transport are difficult. Furthermore, the Lehning et al. (2002) model was parameterized based on data collected at an alpine catchment close to Davos, Switzerland, whereas the Liston et al. (2007) model was parameterized based on data collected at rather smooth hills at a different climate in the US. Our measured densification rates fall right in between the modeled range. For completeness, we re-parameterize the models by fitting the RWT data (Exp. 1-7, Table 1). We obtain the following parameters, β_0 = 2.16, β_1 = 0.034, β_2 = -0.63 and β_3 = 0.97 for the SNOWPACK (Lehning et al., 2002) model (Eq. 1) using the default 'ZWART' parameterization, while D_1 = 17, D_2 = 250 and D_3 = 0.06 are found for the SnowTran-3D (Liston et al., 2007) model (Eq. 2).

3.4.3 Sensitivity to duration and temperature

The experiments with different durations (Experiment 8-9, τ_{exp} = 1 h and 2.5 h, Table 1) and air temperatures (Experiment 10-12, T_a = -12°C, -6°C and -2°C, Table 1) were conducted with a wind speed of $V_{0.4m}$ = 6 m s^{-1} and are spanning a range of densification rates from 1.5 h^{-1} < ϕ_{rate} < 4 h^{-1} (Fig. 9). The effective transport duration τ_t can be interpreted as the average time individual snow crystals are effectively transported by the wind, whereas the experiment duration τ_{exp} (Table 1) is defined as the time during which one box of new snow is slowly added to the wind tunnel simulating precipitation. The transport
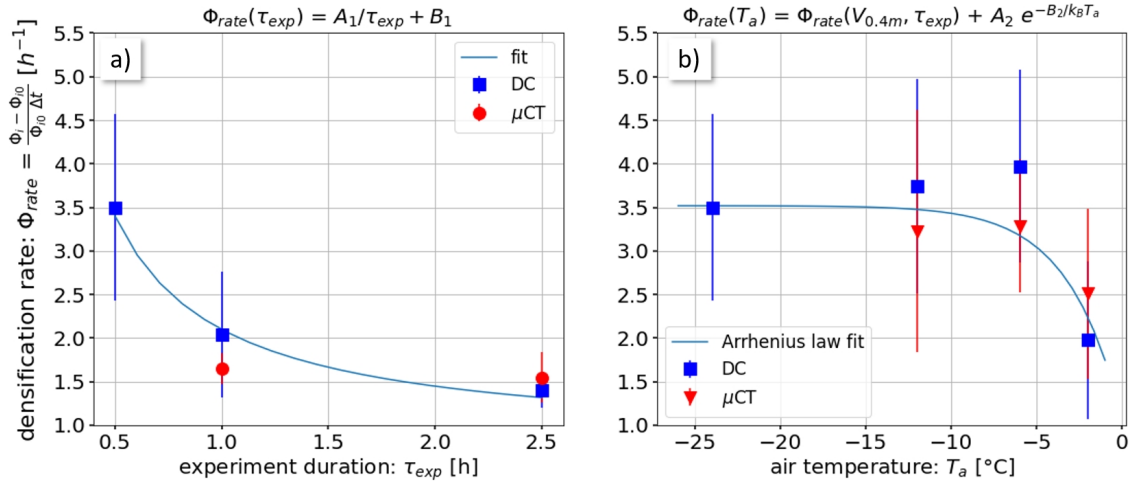
Figure 9. Densification rate as a function of a) the experiment duration τ_{exp} and b) the air temperature T_a including fits.

duration τ_t is difficult to quantify for these experiments. However, τ_t is a function of τ_{exp}, so τ_t can be indirectly controlled by varying the time a box of snow is slowly added to the RWT and thus by τ_{exp}. By reducing this 'precipitation rate' for the

300   Experiments 8 (τ_{exp} = 1 h) and 9 (τ_{exp} = 2.5 h), the effective transport duration τ_t of individual snow grains is increased as they are longer exposed to the wind before ultimately deposited, which was argued to be an effect of additional fragmentation.

The decrease of the densification rate with experiment duration (Fig. 9a) would be consistent with this: Fragmentation should be high initially and decreasing with time, since the most fragile particles break first. If thus fragmentation controls densification, a decrease of the rate as a function of transport duration can be expected as observed in Fig 9a. A simple two

305   parameter fit of a function inverse proportional to the experiment duration is applied to the data in Fig. 9a resulting in

$$\phi_{rate}(\tau_{exp}) = A_1/\tau_{exp} + B_1 \tag{4}$$

with A_1 = 1.30 and B_1 = 0.80 h^{-1}, simply to represent the data points in the experimental range. On physical grounds, the densification rate should tend to zero instead for very long times.

The temperature dependence of the densification rate shows little or no trend for temperatures below T_a < -5°C (Fig. 9b) with

310   values of $\phi_{rate} \approx 3.5$ h^{-1}, while it significantly drops to $\phi_{rate} \approx 2.2$ h^{-1} for higher air temperatures T_a > -5°C (Experiment 12). Cohesion of the snow particles drastically increases for T_a > -5°C as shown by the angle of repose experiments performed by Willibald et al. (2020) and Eidevåg et al. (2022). We hypothesize that cohesion and sintering at higher air temperatures inhibits snow particle transport, saltation and thus fragmentation and snow densification. This hypothesis cannot be proven based on our RWT experiments presented in this study. However, for another RWT study, we simulated precipitation while

315   continuously increasing the air temperature from T_a = -5°C to +2°C. We found that the particle mass flux in the saltation layer gradually decreased and entirely stopped at around -0.5°C to 0°C due to strong cohesion between the new snow crystals on the ground resulting in low density snow accumulations. As in Willibald et al. (2020), we can assume an Arrhenius form for the
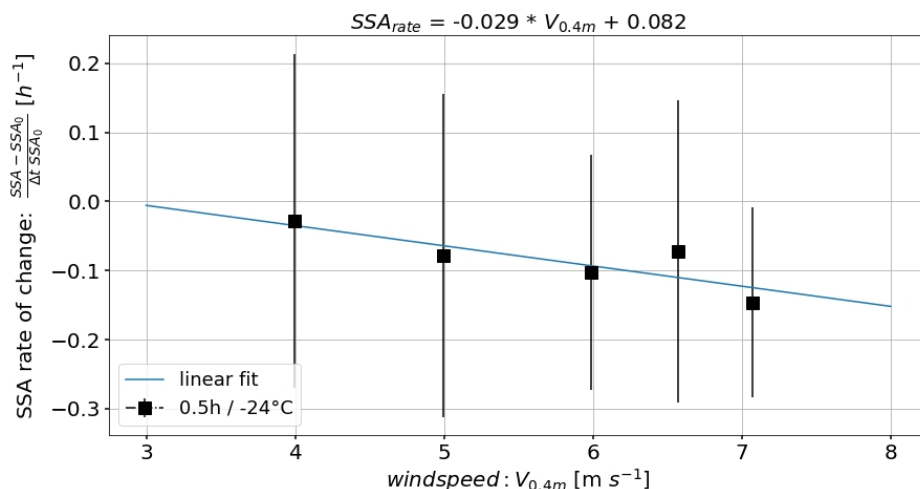
Figure 10. SSA_{rate} as a function of wind speed $V_{0.4m}$ for the experiments 3-7 (Table 1) including a linear fit.

temperature dependency of the densification rate:

$$\phi_{rate}(T_a) = \phi_{rate}(V_{0.4m}, \tau_{exp}) + A_2 e^{-B_2/k_B T_a} \tag{5}$$

320   where $\phi_{rate}(V_{0.4m} = 6\ \mathrm{ms}^{-1}, \tau_{exp} = 0.5\mathrm{h}) = 3.5\ \mathrm{h}^{-1}$ is the mean initial densification rate for $T_a < -5°C$, $A_2 = -3.12\ 10^{38}\ \mathrm{h}^{-1}$
and $B_2 = 2.06$ eV are constants, and $k_B = 8.6\ 10^{-5}$ eVK^{-1} the Boltzmann constant, thus the air temperature in Kelvin must
be used in Eq. 5. While the inferred parameterization $\phi_{rate} = f(T_a)$ is based on limited data and a limited range of parameter
validity, the data highlights a similar temperature effect in wind-deposited snow observed here and ballistically deposited snow
governing the angle of repose (Willibald et al. 2020).

325   ## 3.5 SSA rate

The impact of wind speed, transport duration and air temperature on the SSA rate, defined as $SSA_{rate} = (SSA\text{-}SSA_0)$ /
$(SSA_0\ \Delta t)$ is discussed in analogy to the densification rate.

3.5.1   Dependence on wind speed and involved mechanisms

Fig. 10 shows that the SSA_{rate} decreases from SSA_{rate} = -0.03 h^{-1} to SSA_{rate} = -0.16 h^{-1} with increasing wind speed
330   ($V_{0.4m}$ = 4 - 7.1 ms^{-1}). Although the SSA decrease is small relative to the error bars (Fig. 6c-d, partially due to the spatial SSA
variability, Fig. 7b), the data point for $V_{0.4m}$ = 7.1 ms^{-1} confirms a significant deviation from SSA_{rate} = 0 h^{-1}. These rates
are up to one order of magnitude higher than the rates ($SSA_{rate} \approx$ -0.01 h^{-1}) found by Schleef et al. (2014a) for isothermal
metamorphism. Our result substantiates the findings of Cabanes et al. (2003) who found wind to increase the rate of SSA
decrease which was not further quantified due to limited data.

335 Fragmentation of dendritic crystals cannot cause the measured reduction in the SSA, because the resulting additional surfaces would lead in an increase in the ice surface and thus the SSA. Different mechanisms remain that may be responsible for the SSA decrease: i) Sublimation: Some of the smallest fragments and dendrites entirely disappear because of sublimation (Groot-Zwaaftink et al., 2013). This assumption is supported by the increase in relative humidity as shown in Fig. 2. ii) Vapor re-deposition: Recrystallisation of humidity at the surface of suspended snow particles likely results in an average grain
340 growth similar to isothermal metamorphism of new snow (e.g., Schleef et al., 2014a). These first two mechanisms we refer to as airborne snow metamorphism, in analogy to sublimation and re-deposition processes occurring in deposited snow. iii) Particle separation: This effect has not yet been documented for snow, however, likely occurs when larger fragments remain in saltation close to the snow surface (Fig. 3) whereas the smallest fragments transition into suspension (Nishimura and Nemoto, 2005), forming a blowing snow layer (Palm et al., 2017). In the field, these small blowing snow particles may disappear due
345 to sublimation or being blown out of an area of interest (Palm et al., 2017). In a non-sealed RWT, small particles may be also blown out at the inlet (Fig. 1a). Thin layers of fine snow dust were found after the experiments outside the RWT in proximity to the inlet (Fig. 1a) supporting that particle separation occurs in our experiments.

The minor, potentially linear increase of the negative SSA rates (in absolute values) in Fig. 10 suggests an amplification of the above assumed processes of airborne metamorphism and particle separation with increasing wind speed. We argue that
350 higher airborne particle concentrations at higher wind speeds allow an increasing number of particles experiencing airborne metamorphism. Higher mass fluxes also result in an increasing number of smaller particles in higher air layers (Walter et al., 2017) that may partially be blown out of the inlet, thus likely resulting in intensified particle separation.

3.5.2 Sensitivity to duration and temperature

The SSA_{rate} for the different experiment durations (Experiment 8-9, τ_{exp} = 1 h and 2.5 h, Table 1) and air temperatures
355 (Experiment 10-12, T_a = -12°C, -6°C and -2°C, Table 1) span a range of -0.3 h^{-1} < SSA_{rate} < 0.01 h^{-1} (Fig. 11). Regarding the dependency of SSA_{rate} on the experiment transport duration τ_{exp} (Fig. 11a) a mean value of SSA_{rate} = -0.048 h^{-1} is found. Due to the limited data and the relatively large error bars, no firm conclusion can be drawn on the dependency of SSA_{rate} on the transport duration or τ_{exp} based on Fig. 11a.

A different picture appears for the dependency of the SSA_{rate} on the air temperature T_a (Fig. 11b), where a constant value
360 of SSA_{rate} = -0.07 h^{-1} is measured for T_a < -5°C, while a significant drop to a value of SSA_{rate} = -0.32 h^{-1} is measured for Experiment 12 at T_a = -2°C. Despite the rather large error bars (see Section 3.3), the significant change in SSA_{rate} for T_a > -5°C has individually been measured by two independent instruments, with good agreement between the SSA_{rate} values determined from the IceCube (blue squares) and the μCT (red triangles) measurements. While stronger cohesion was likely the reason for the reduced densification rate ϕ_{rate} for T_a > -5°C (Fig. 9b), enhanced sublimation and vapor re-deposition at
365 higher air temperatures (Palm et al., 2017) may explain intensified airborne snow metamorphism and thus a stronger reduction of the SSA values in this case (e.g. Harris et al., 2023). Like for the densification rate (Eq. 5), we assume an Arrhenius form
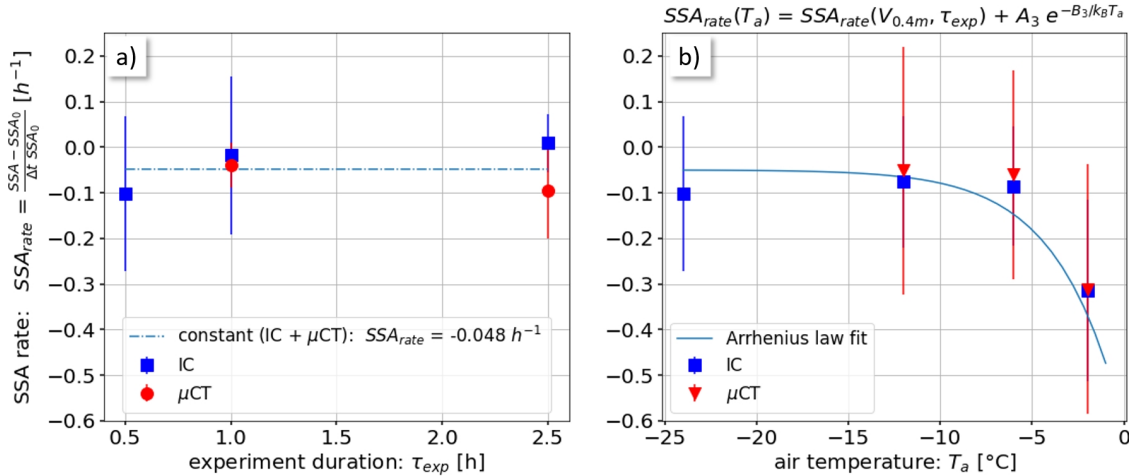
Figure 11. SSA_{rate} as a function of a) the experiment duration τ_{exp} and b) the air temperature T_a including an exponential fit.

(Willibald et al., 2020) for the temperature dependency of the SSA rate:

$$SSA_{rate}(T_a) = SSA_{rate}(V_{0.4m}, \tau_{exp}) + A_3 e^{-B_3/k_B T_a} \tag{6}$$

where $SSA_{rate}(V_{0.4m} = 6 \text{ m s}^{-1}, \tau_{exp} = 0.5\text{h}) = -0.07 \text{ h}^{-1}$ is the mean initial SSA_{rate} for $T_a < -5°C$, $A_3 = -5.4 \text{ } 10^{33} \text{ h}^{-1}$ and
370    $B_3 = 1.8 \text{ eV}$ are constants, and the air temperature T_a in Kelvin must be used in Eq. 6. Whether the proposed parameterization of Eq. 6 is valid for different wind speeds $V_{0.4m}$ and experiment durations τ_{exp} must be tested in future studies. Similar results of a decreasing SSA with increasing wet-bulb air temperature were found by Yamaguchi et al. (2019) for precipitation particles under low wind conditions, while also Schleef et al. (2014) found that the SSA decay increased with higher air temperatures for isothermal snow metamorphism.

375 **3.6   Particle separation and airborne snow metamorphism**

To further substantiate the previous hypotheses that airborne snow metamorphism and particle separation play a role for the evolution of the SSA under the influence of wind we provide sensitivity evaluations.

3.6.1   Particle separation

For Experiment 9 we also collected some of the accumulated dust outside of the RWT for μCT analysis, in addition to the initial
380   snow and the snow deposited in the RWT. A metric for the particle size distribution can be derived from the μCT images by filling the 3D ice matrix with inscribed spheres of different diameters D (Hildebrand and Rüegsegger, 1997). Figure 12a shows the frequency distribution of the spheres for the three snow samples taken during Experiment 9 (Table 1). Similar distributions were obtained for all experiments (5-12) where μCT samples were taken. The new snow produced in the Snowmaker (cyan squares) shows a peak in the distribution at a size of $D_{peak} = 80 \text{ } \mu$m and only few particles at a maximum size of $D_{max} = 300$
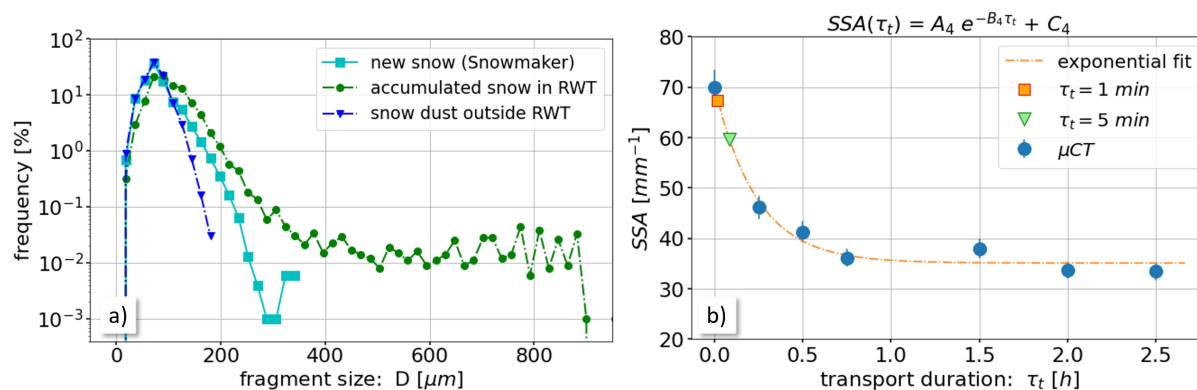
Figure 12. a) Particle size distributions derived from μCT measurements for the fresh snow produced in the Snowmaker (cyan squares), the wind affected snow sampled in the accumulation area (green dots), and for snow dust that has been blown out of the RWT for experiment 9 (blue triangles). b) Exponential SSA decrease measured for the supplementary experiment on long transport durations τ_t including estimates for the effective transport durations of the main experiments (orange square and green triangle).

385   μm. A general shift of the distribution towards larger particles sizes ($D_{peak} = 100\ \mu$m), along with a reduction in the frequency of smaller particles (20 μm < D < 80 μm) and a maximum size increase to $D_{max} = 900\ \mu$m is found for the accumulated snow after wind exposure (green dots). This shift indicates that smaller particles, e.g. fragmented dendrites are removed from the system likely due to sublimation and particle separation where, for the latter, the smallest fragments are partially blown out of the RWT. The increased appearance of particles with D > 300μm after wind exposure may also be the result of particle

390   separation, where the largest particles remain in saltation and are finally deposited in the accumulation area. The general shift of the particle size distribution towards larger spheres due to particle separation and airborne metamorphism is in line with our finding of a decreasing SSA as discussed in the previous Section.

     The existence of the process of particle separation in our RWT experiments is substantiated by the particle size distribution of a small snow dust sample taken outside of the RWT (blue triangles, Fig. 12a). Most of these snow dust particles are within

395   a range of 20μm < D < 120μm and coincide exactly with the size range where a depletion is found for the wind affected snow (green circles) relative to the initial new snow (cyan squares). Generally, particle sizes in snow saltation layers were experimentally (Gromke et al., 2014) and numerically (Melo et al., 2021) found to strongly decrease with increasing height above the ground, being the reason for the snow dust being blown out at the inlet. Similar processes of particle separation occur during Saharan dust events, where micrometer sized particles are transported hundreds or thousands of kilometers whereas

400   larger sand grains are predominantly redeposited locally (e.g. van der Does et al., 2016). For ice deserts, sublimation of blowing snow particles is resulting in a significant snow mass loss for Antarctica (Palm et al. 2017). Apparent similarities are also found between our wind affected particle size distributions and the model results from Comola et al. (2017). While this analysis of size distributions is consistent with particle separation and the hypothesized impact on SSA decay, we acknowledge the known difficulties of the involved size distribution (Löwe et al., 2011) for characterizing the full size complexity of dendritic crystals.

405   A further analysis likely requires a better metric to discern fragmentation and separation.

3.6.2 Airborne snow metamorphism

In our main experiments, the SSA decay in the deposit (Fig. 6c-d, 10 and 11) is only moderate and the hypothesized process of airborne snow metamorphism through continuous sublimation and vapor re-deposition is difficult to verify. To illustrate the existence of airborne metamorphism and its relevance for the SSA decrease, a sensitivity RWT experiment was conducted where a single portion (600g) of dendritic new snow from the snowmaker was added to the initially empty RWT at T_{air} = -20°C, while the wind speed was set to the maximum of $V_{0.4m} = 8 \ ms^{-1}$ (Experiment 14). In this way we were able to maintain a large portion of the particles in suspension over long periods without deposition. Snow was periodically collected from the suspended particle phase by capturing particles with a small bag for μCT analysis out of the airstream. For this experiment, the RWT was sealed as good as possible to avoid particles being blown out of the RWT.

Fig. 12b shows the considerable decrease of the SSA with increasing transport duration τ_t. Here, the real transport duration for the particles is used instead of the previously (Fig. 9a and 11a) used experiment duration τ_{exp}, as it can be assumed that the particles that are captured out of the flow after some time were mobile the majority of the preceding time. The decrease can be empirically described by an exponential function:

$$SSA(\tau_t) = A_4 e^{-B_4 \tau_t} + C_4 \tag{7}$$

where A_4 = 34.5 mm^{-1}, B_4 = 4.2h and C_4 = 35.2 mm^{-1} are constants. The observed change of the snow microstructure from highly dendritic crystals to continuously growing rounded grains together with the strong decrease in the SSA demonstrates the existence of airborne snow metamorphism, with an impact on the SSA decrease which depends on transport duration.

We can compare our previous results with Figure 12b by the following reasoning. The average transport duration τ_t for the main RWT experiments can be roughly estimated when dividing the experiment duration (τ_{exp}) (Table 1) by the number of snow supplies ($\approx$30) when simulating precipitation. This leads to an estimate of $\tau_t \approx$ 1 min for the 0.5 h lasting experiments and $\tau_t \approx$ 5 min for the 2.5 h lasting experiment. The corresponding SSA reductions are shown in Fig. 12b, implying a reduction of the specific surface area from SSA = 70 mm^{-1} to SSA = 67 mm^{-1} for the 0.5 h experiments (orange square), and a reduction to SSA = 60 mm^{-1} for the 2.5 h experiment (green triangle in Fig. 12b). The corresponding SSA rates are in both cases $\phi_{rate} \approx -0.1 h^{-1}$ which is consistent with the rates measured for the main RWT experiments (Fig. 10 and Fig. 11). We thus expect these rates to be a real signature of airborne snow metamorphism, that is concealed in the uncertainties due to the short transport durations, spatial variability and measurement uncertainties in our experiments.

4 Conclusions

Ring wind-tunnel experiments were performed to investigate the evolution of the surface snow microstructure (specific surface area and density), under wind for different transport conditions (wind speed, air temperature and transport duration) in a controlled cold laboratory environment. The results provide novel insight into the link between deposited snow, atmospheric conditions and airborne snow particles.

The measured increase of the densification rate with increasing wind speed (Fig. 8) significantly differs from previous model parameterizations that are exclusively based on field studies. Therefore, a re-parameterization of these models from our data is

440 derived. The dissipated energy upon particle impact (Fig. 5) suggests that increasing fragmentation of dendritic snow crystals is the reason for increasing densities with increasing wind speeds. A decreasing densification rate with increasing transport duration (Fig. 9a) is consistent with that, since the initial fragmentation must be higher where the most fragile dendrites or particles break first. For higher air temperatures (T_a > -5°C), the densification rate show a marked decrease compared to the rather constant rates at lower temperatures (Fig. 9b). This was attributed to the effect of enhanced cohesion (or sintering) which

445 on one hand inhibits particle transport and on the other hand reduces the packing fraction directly close to the melting point.

The observed slight increase of the SSA rate in absolute values (Fig. 10) with increasing wind velocity is attributed to the processes of airborne metamorphism and particle separation. Both are expected to be amplified with increasing wind velocities. Similar to the densification rate, the SSA decrease rate was approximately constant at low air temperatures (T_a < -5°C) and markedly increased (in absolute values) for air temperatures (T_a > -5°C). The significance of airborne metamorphism, where

450 sublimation and vapor re-deposition result in a SSA reduction, was demonstrated in a sensitivity experiment which revealed a strong SSA decrease of the airborne particles for long transport durations (Fig. 12b). The process of particle separation, where the smallest particles in suspension are blown out of the wind tunnel, was exemplified by an analysis of the particle size distribution of a small snow dust sample taken outside from the wind tunnel roof; however, its relevance for real natural blowing snow events remains debatable. Although the processes of airborne snow metamorphism and particle separation are

455 certainly not perfectly reproduced in the RWT relative to real field conditions due to the uncontrolled exchange of air with the outside of the RWT at the inlet, they both occur during natural aeolian snow transport. Therefore, the observed SSA decrease (Fig. 10, 11 and 12b) provides a first assessment of the impact of these processes on the SSA, however, the magnitudes of the SSA decrease must be verified in future studies.

Overall, we have demonstrated that our setup of a ring wind-tunnel in a cold laboratory allows for revealing the relevant

460 processes responsible for the densification and SSA decrease of snow under wind. The presented results highlight the complexity of the involved processes and how they may affect the resulting surface snow microstructure. However, more detailed studies on the individual processes, i.e. particle fragmentation, airborne metamorphism and particle separation are required to fully understand and quantify their impact. Our study is the first step to pinpoint weaknesses and improve existing models for the evolution of surface snow under different wind and atmospheric conditions. This is relevant for applications in radiative

465 transfer (albedo), the exchange of chemical species with the atmosphere, snow hydrology or avalanche prediction. Generally, any layer within a snowpack originates from a surface snow layer. A detailed understanding of the initial microstructure of the surface layer therefore impacts also the evolution of snow layers in the snowpack throughout its seasonal (or perennial) lifetime.

470 *Data availability.* The data will be made available after the manuscript is officially published.

Author contributions. BW, HW and SW conducted the experiments, BW analysed the data, created the figures, and prepared the manuscript. HW analysed the high-speed camera data. HL provided theoretical input and edited the manuscript.

Competing interests. The authors declare no competing interests.

Acknowledgements. The authors acknowledge Hongxiang Yu for providing OpenFoam simulations of the air flow and the particle saltation layer in the ring wind tunnel, Matthias Jaggi for the cold laboratory support, and Christian Sommer and Charles Fierz for the design and realization of the ring wind tunnel system.

475

References

Bartlett, S. J., Rüedi, J.-D., Craig, A., and Fierz, C., (2008). Assessment of techniques for analyzing snow crystals in two dimensions. Annals of Glaciology, 48, 103–112.

480 Brun, E., Martin, E., and Spiridonov, V. (1997). Coupling a multi-layered snow model with a GCM, Ann. Glaciol., 25, 66–72.

Cabanes, A., L. Legagneux, and F. Domine (2003). Rate of Evolution of the Specific Surface Area of Surface Snow Layers, Environmental Science and Technology, vol.37, issue.4, pp.661-66610, 2003. $doi : 10.1021/es025880r$

Cho G, Dodds J, Santamarina J (2006). Particle shape effects on packing density, stiffness, and strength: natural and crushed sands. J Geotech Geoenviron Eng 132(5):591–602

485 Comola, F., J. F. Kok, J. Gaume, E. Paterna, and M. Lehning (2017), Fragmentation of wind-blown snow crystals, Geophys. Res. Lett., 44, 4195–2403, $doi : 10.1002/2017GL073039$

Dai, X., Huang, N. (2014). Numerical simulation of drifting snow sublimation in the saltation layer. Sci Rep 4, 6611 $https : //doi.org/10.1038/srep06611$

Domine, F., Picard, G., Morin, S., Barrere, M., Madore, J.-B., Langlois, A. (2019). Major issues in simulating some Arctic
490 snowpack properties using current detailed snow physics models: Consequences for the thermal regime and water budget of permafrost. Journal of Advances in Modeling Earth Systems, 11, 34–44. $https : //doi.org/10.1029/2018MS001445$

Eidevåg, T., Thomson, E., Kallin, D. et al (2022). Angle of repose of snow: An experimental study on cohesive properties. Cold Regions Science and Technology, 194. $http : //dx.doi.org/10.1016/j.coldregions.2021.103470$

Fierz, C., Armstrong, R. L., Durand, Y., Etchevers, P., Greene, E., McClung, D. M., Sokratov, S. A. (2009). The international
495 classification for seasonal snow on the ground. Prepared by the ICSI-UCCS-IACS working group on snow classification. (IHP-VII technical documents in hydrology). UNESCO; IHP.

Flanner, M. G., and C. S. Zender (2006). Linking snowpack microphysics and albedo evolution, J. Geophys. Res., 111, D12208, $doi : 10.1029/2005JD006834$

Gallet, J.-C., Domine, F., Zender, C.S. and Picard, G. (2009). Measurement of the specific surface area of snow using infrared
500 reflectance in an integrating sphere at 1310 and 1550 nm. Cryosphere, 3(2), 167–182.

Gallet, J.-C., Domine, F., Arnaud, L., Picard, G. and J. Savarino (2010). Vertical profile of the specific surface area and density of the snow at Dome C and on a transect to Dumont 'Urville, Antarctica – albedo calculations and comparison to remote sensing products. Cryosphere, 5, 631–649.

Garrett, T. J., and S. E. Yuter (2014). Observed influence of riming, temperature, and turbulence on the fall velocity of solid
505 precipitation, Geophys. Res. Lett., 41, 6515–6522, $doi : 10.1002/2014GL061016$

Golubev V.N., Sokratov S.A. (2004). Regular packing of grains as a model of snow structure. — Annals of Glaciology, v. 38, 2004, p. 25-29. 25.

Gromke, C., Horender, S., Walter, B., Lehning, M. (2014). Snow particle characteristics in the saltation layer. Journal of Glaciology, 60(221), 431-439. $https://doi.org/10.3189/2014JoG13J079$

510   Groot Zwaaftink, C. D., Mott, R., and Lehning, M. (2013). Seasonal simulation of drifting snow sublimation in Alpine terrain. Water Resour. Res. 49, 1581–1590. $doi:10.1002/wrcr.20137$

Hagenmuller, P, G Chambon, B Lesaffre, F Flin, M Naaim (2013) Energy-based binary segmentation of snow microtomographic images. Journal of Glaciology 59 (217), 859-873

Hagenmuller, P., Matzl, M., Chambon, G., and Schneebeli, M. (2016) Sensitivity of snow density and specific surface area mea-
515   sured by microtomography to different image processing algorithms, The Cryosphere, 10, 1039–1054, $https://doi.org/10.5194/tc-10-1039-2016$

Harris Stuart, R., Faber, A.-K., Wahl, S., Hörhold, M., Kipfstuhl, S., Vasskog, K., Behrens, M., Zuhr, A. M., and Steen-Larsen, H. C. (2023) Exploring the role of snow metamorphism on the isotopic composition of the surface snow at EastGRIP, The Cryosphere, 17, 1185–1204, $https://doi.org/10.5194/tc-17-1185-2023$

520   Heggli, M., Köchle, B., Matzl, M., Pinzer, B. R., Riche, F., Steiner, S., Steinfeld, D., Schneebeli, M. (2011). Measuring snow in 3-D using X-ray tomography: assessment of visualization techniques. Annals of Glaciology, 52(58), 231-236. $https://doi.org/10.3189/172756411797252202$

Hildebrand, T. and P. Rüegsegger (1997) A new method for the model-independent assessment of thickness in three- dimensional images. J. Microsc., 185(1), 67–75.

525   Lehning, M., Bartelt, P., Brown, R.L., Fierz, C., and Satyawali, P.K. (2002). A physical SNOWPACK model for the Swiss avalanche warning, Part II. Snow microstructure, Cold Regions Science and Technology 35, 2002, 147–167.

Libbrecht, K.G., (2005) The Physics of Snow Crystals, Rep. Prog. Phys. 68 855

Liston, G., Haehnel, R., Sturm, M., Hiemstra, C., Berezovskaya, S., Tabler, R. (2007). Simulating complex snow distributions in windy environments using SnowTran-3D. Journal of Glaciology, 53(181), 241-256. $doi:10.3189/172756507782202865$

530   Löwe, H., Spiegel, J. K., and Schneebeli, M. (2011) Interfacial and structural relaxations of snow under isothermal conditions, J. Glaciol., 57, 499–510.

Martin, J. and Schneebeli, M.: Impact of the sampling procedure on the specific surface area of snow measurements with the IceCube, EGUsphere [preprint], $https://doi.org/10.5194/egusphere-2022-501, 2022$

Melo, D. B., Sharma, V., Comola, F., Sigmund, A., Lehning, M. (2022). Modeling snow saltation: The effect of grain size and interparticle cohesion. Journal of Geophysical Research: Atmospheres, 127, e2021JD035260. $https://doi.org/10.1029/2021JD035260$

Meredith, M., M. Sommerkorn, S. Cassotta, C. Derksen, A. Ekaykin, A. Hollowed, G. Kofinas, A. Mackintosh, J. Melbourne-Thomas, M.M.C. Muelbert, G. Ottersen, H. Pritchard, and E.A.G. Schuur, 2019: Polar Regions. In: IPCC Special Report on the Ocean and Cryosphere in a Changing Climate [H.-O. Pörtner, D.C. Roberts, V. Masson-Delmotte, P. Zhai, M. Tignor, E. Poloczanska, K. Mintenbeck, A. Alegría, M. Nicolai, A. Okem, J. Petzold, B. Rama, N.M. Weyer (eds.)]. Cambridge University Press, Cambridge, UK and New York, NY, USA, pp. 203–320. https://doi.org/10.1017/9781009157964.005

Mott, R., Vionnet, V., and Grünewald, T. (2018) The Seasonal Snow Cover Dynamics: Review on Wind-Driven Coupling Processes, Front. Earth Sci., 6, 197, $https://doi.org/10.3389/feart.2018.00197$

Nishimura, K., and M. Nemoto (2005). Blowing snow at Mizuho station, Antarctica, Phil. Trans. R. Soc. A, 363(1832), 1647–1662.

Nishimura, K., C. Yokoyama, Y. Ito, M. Nemoto, F. Naaim-Bouvet, H. Bellot, and K. Fujita (2014). Snow particle velocities in drifting snow, J. Geophys. Res. Atmos., 119, 9901–9913, $doi:10.1002/2014JD021686$

Palm, S. P., Kayetha, V., Yang, Y., and Pauly, R. (2017) Blowing snow sublimation and transport over Antarctica from 11 years of CALIPSO observations, The Cryosphere, 11, 2555–2569, $https://doi.org/10.5194/tc-11-2555-2017$

Parteli, E.J.R., Schmidt, J., Blümel, C., Wirth, K.-E., Peukert, W. and Pöschel, T. (2014), 'Attractive particle interaction forces and packing density of fine glass powders', Scientific Reports 4: 6227; $doi:10.1038/srep06227$

Pinzer B and Schneebeli M (2009) Snow metamorphism under alternating temperature gradients: morphology and recrystallization in surface snow. Geophys. Res. Lett., 36(23) $doi:10.1029/2009GL039618$

Pomeroy, J. W., H. G. Jones (1996) Windblown snow: Sublimation, transport and changes to polar snow, Chemical Exchange Between the Atmosphere and Polar Snow, NATO ASI Ser. I, 43 E. Wolff, R. Bales, 453– 489, Springer-Verlag, New York

Proksch, M., Löwe, H., Schneebeli, M. (2015). Density, specific surface area, and correlation length of snow measured by high-resolution penetrometry. Journal of Geophysical Research F: Earth Surface, 120(2), 346-362. $https://doi.org/10.1002/2014JF003266$

Proksch, M., Rutter, N., Fierz, C., and Schneebeli, M. (2016): Intercomparison of snow density measurements: bias, precision, and vertical resolution, The Cryosphere, 10, 371–384, $https://doi.org/10.5194/tc-10-371-2016$

Rignot, E.; Thomas, R.H. Mass Balance of Polar Ice Sheets. Science 2002, 297, 1502–1506.

Sato, T., K. Kosugi, S. Mochizuki, and M. Nemoto (2008). Wind velocity dependences of fracture and accumulation of snowflakes on snow surface, Cold Reg. Sci. Technol., 51(2), 229–239.

565 Schleef, S., Löwe, H., Schneebeli, M. (2014a). Influence of stress, temperature and crystal morphology on isothermal densification and specific surface area decrease of new snow. Cryosphere, 8(5), 1825-1838. $https://doi.org/10.5194/tc-8-1825-2014$

Schleef, S., Jaggi, M., Löwe, H., Schneebeli, M.(2014b). An improved machine to produce nature-identical snow in the laboratory, J. Glaciol., 60, 94–102.

570 Schmidt, R. (1982). Vertical profiles of wind velocity, snow concentration, and humidity in blowing snow, Boundary Layer Meteorol., 23(2), 223–246. Schweizer, J., Jamieson, J.B., Schneebeli, M., (2003). Snow avalanche formation. Reviews of Geophysics 41(4), 25 pp.

Seligman, G. (1936). Snow structure and ski fields. 1980 edition by International Glaciological Society, Cambridge, Cambridge, UK, 555 pp.

575 Sokratov, S., Sato, A. (2001). The effect of wind on the snow cover. Annals of Glaciology, 32, 116-120. $doi : 10.3189/172756401781819436$

Sommer, C. G., Lehning, M., and Fierz, C. (2017). Wind tunnel experiments: saltation is necessary for wind-packing, J. Glaciol., 63, 950–958, $https://doi.org/10.1017/jog.2017.53$

Sommer, C. G., Lehning, M., and Fierz, C. (2018). Wind Tunnel Experiments: Influence of Erosion and Deposition on Wind-580 Packing of New Snow, Front. Earth Sci., 6, 4, $https://doi.org/10.3389/feart.2018.00004$

Sommerfeld H., Koch, C., Schwarz A., Beck, C. (2021) High velocity measurements of particle rebound characteristics under erosive conditions of high-pressure compressors, Wear 470-471 (2021) 203626

Sugiura, K., Maeno, N. Wind-Tunnel Measurements Of Restitution Coefficients And Ejection Number Of Snow Particles In Drifting Snow: Determination Of Splash Functions. Boundary-Layer Meteorology 95, 123–143 (2000).
585 $https://doi.org/10.1023/A : 1002681026929$

van der Does, M., Korte, L. F., Munday, C. I., Brummer, G.-J. A., and Stuut, J.-B. W.: Particle size traces modern Saharan dust transport and deposition across the equatorial North Atlantic, Atmos. Chem. Phys., 16, 13697–13710, $https://doi.org/10.5194/acp-16-13697-2016$

Vionnet, V., Brun, E., Morin, S., Boone, A., Faroux, S., Le Moigne, P., Martin, E., and Willemet, J.-M. (2012). The detailed 590 snowpack scheme Crocus and its implementation in SURFEX v7.2, Geosci. Model Dev., 5, 773–791, $https://doi.org/10.5194/gmd-5-773-2012$

Walter B, Gromke C, Leonard K, Clifton A, Lehning M (2012a). Spatially resolved skin friction velocity measurements using Irwin sensors: a calibration and accuracy analysis. J Wind Eng Ind Aerodyn 144:104–106. $doi : 10.1016/j.jweia.2012.02.018$

Walter B, Gromke C, Leonard K, Manes C, Lehning M(2012b). Spatio-temporal surface shear stress variability in live plant 595 canopies and cube arrays. Boundary-Layer Meteorol 143(2):337–356. $doi : 10.1007/s10546-011-9690-5$

Walter B, Gromke C, Lehning M (2012c). Shear stress partitioning in live plant canopies and modifications to Raupach's model. Boundary-Layer Meteorol 144(2):217–241. $doi: 10.1007/s10546 - 012 - 9719 - 4$

Walter B, Horender S, Voegeli C, Lehning M (2014). Experimental assessment of Owen's second hypothesis on surface shear stress induced by a fluid during sediment saltation. Geophys Res Lett 41:6298–6305

600   Walter B, Voegeli C, Horender S (2017) Estimating sediment mass fluxes on surfaces sheltered by live vegetation, Boundary-Layer Meteorol 163: 273. doi.org/10.1007/s10546-016-0224-z

Warren SG. (2019) Optical properties of ice and snow. Phil. Trans. R. Soc. A377: 20180161.
$http://dx.doi.org/10.1098/rsta.2018.0161$

Willibald, C.; Löwe, H.; Theile, T.; Dual, J.; Schneebeli, M. (2020). Angle of repose experiments with snow: role of grain
605   shape and cohesion. Journal of Glaciology, $doi: 10.1017/jog.2020.36$

Woods, C. P., M. T. Stoelinga, and J. D. Locatelli (2008). Size spectra of snow particles measured in wintertime precipitation in the Pacific Northwest, J. Atmos. Sci., 65(1), 189–205

Yamaguchi, S., Ishizaka, M., Motoyoshi, H., Nakai, S., Vionnet, V., Aoki, T., Yamashita, K., Hashimoto, A., and Hachikubo, A. (2019). Measurement of specific surface area of fresh solid precipitation particles in heavy snowfall regions of Japan, The
610   Cryosphere, 13, 2713–2732, $https://doi.org/10.5194/tc - 13 - 2713 - 2019$

Yu, H., Li, G., Walter, B., Lehning, M., Zhang, J., and Huang, N.: Wind conditions for snow cornice formation in a wind tunnel, The Cryosphere, 17, 639–651, $https://doi.org/10.5194/tc - 17 - 639 - 2023, 2023$